CARDIFF UNIVERSITY
PRIFYSGOL CAERDYDD

ORCA – Online Research @ Cardiff

This is an Open Access document downloaded from ORCA, Cardiff University's institutional repository:https://orca.cardiff.ac.uk/id/eprint/188807/

This is the author's version of a work that was submitted to / accepted for publication.

Citation for final published version:

Ruiz, H.J. Vargas, Naess, T., Aravind, B., Laera, D., Lartigue, G., Mashruk, S., Valera-Medina, A. and Gicquel, L. 2026. Large Eddy Simulation Cell-by-Cell quantification of nitrogen oxide sub-mechanisms in premixed ammonia-air flames with differentiated hydrogen injection. Combustion and Flame 292 , 115182. 10.1016/j.combustflame.2026.115182

Publishers page: https://doi.org/10.1016/j.combustflame.2026.115182

Please note:
Changes made as a result of publishing processes such as copy-editing, formatting and page numbers may not be reflected in this version. For the definitive version of this publication, please refer to the published source. You are advised to consult the publisher's version if you wish to cite this paper.

This version is being made available in accordance with publisher policies. See http://orca.cf.ac.uk/policies.html for usage policies. Copyright and moral rights for publications made available in ORCA are retained by the copyright holders.

Vargas Ruiz et al.

Large Eddy Simulation Cell-by-Cell Quantification of Nitrogen Oxide Sub-Mechanisms in Premixed Ammonia-Air Flames with Differentiated Hydrogen Injection

H. J. Vargas Ruiz[a,b,*], T. Naess[a], B. Aravind[c], D. Laera[a,d], G. Lartigue[b], S. Mashruk[c], A. Valera-Medina[c], L. Gicquel[a]

[a] *CERFACS, 42 avenue Gaspard Coriolis, 31057 Toulouse, France*
[b] *TotalEnergies, Jean Féger Scientific and Technical Center, 64000, Pau, France*
[c] *College of Physical Sciences and Engineering, Cardiff University, UK*
[d] *Department of Mechanics, Mathematics and Management, Polytechnic University of Bari, Via Orabona 4, 70125 Bari, Italy*

Abstract

Ammonia-hydrogen fuel blends are currently being investigated as a promising technical solution for gas turbine decarbonization, yet NO_x emissions pose critical challenges for industrial deployment. In the present work, joint Large Eddy Simulations (LES) and experimental investigations are proposed to study the NO_x formation mechanisms in premixed ammonia-hydrogen swirled flames enriched with separate hydrogen injection. The target configuration is the experimental setup developed at Cardiff University. Four test points operated at atmospheric pressure and characterized by the same global 70/30 NH_3/H_2 volumetric fuel composition but different equivalence ratios, *i.e.*, 0.65, 0.8, 1.0, and 1.2, are compared. LES performed using the multi-fuel Thickened Flame turbulent combustion model (MF-TFLES), coupled with finite rate chemistry, show good agreement with experimental PLIF NO and OH* chemiluminescence measurements. This validates the capability of the numerical model to accurately reproduce both the flame structure and the emissions distribution.

Cell-by-Cell (CBC) chemical analysis demonstrates that the fuel-NO pathways dominate NO formation despite hydrogen's enhancement of local reactivity through preferential diffusion and superadiabatic effects under lean conditions. The HNO route constitutes the primary formation pathway, while the NH_i and thermal NO contributions remain limited across all operating points. Hydrogen addition intensifies overall reactivity and locally increases NO production but does not alter the dominance of ammonia-derived chemistry over thermal pathways.

Exhaust NO emissions peak at $\phi = 0.8$ and approach zero at $\phi = 1.2$, driven by the presence of unburnt ammonia under rich conditions. The reburn mechanism actively consumes NO at all equivalence ratios but exhibits maximum effectiveness at $\phi = 0.65$, preventing the highest NO production rates from translating to peak exhaust emissions

which are observed at $\phi = 0.8$. N_2O formation occurs upstream in reactive zones before thermal decomposition to N_2, with negligible exhaust concentrations except under very lean conditions at $\phi = 0.65$.

Keywords: Ammonia, Hydrogen, Large Eddy Simulations, Combustion, NO PLIF, Multi-fuel, Thickened Flame model, Gas turbines, NO, Pollutants, Cell-by-Cell

Novelty and significance statement

This research presents novel OH* chemiluminescence and NO PLIF measurements on swirling ammonia-hydrogen flames with differentiated fuel injection. The recently introduced multi-fuel thickened flame turbulent combustion model (MF-TFLES) is applied to LES of complex ammonia-hydrogen-air swirling flames with heterogeneous fuel composition obtained via a differentiated injection strategy. Based on a finite rate chemistry methodology, Cell-by-Cell quantification of individual reaction contributions allows to identify spatial distribution of pollutant formation sub-mechanisms. This understanding address the primary challenge of NO_x control in ammonia-hydrogen combustion, enabling industrial adoption of carbon-free fuel systems.

1. Introduction

The ubiquitous need to decarbonize the current energy mix and mitigate carbon dioxide emissions in transport applications points to ammonia as a viable surrogate to hydrogen [1], particularly in sectors like power generation, through gas turbines [2, 3] and the transport industry, through internal combustion engines (ICE) [4, 5, 6]. Indeed, although hydrogen also offers a carbon-free combustion option, its transport is logistically challenging due to its low energy density and high flammability [7]. Conversely, ammonia is more readily handled and benefits from an existing and well-established logistic infrastructure. Nevertheless, ammonia typically requires mixing with more reactive fuels due to its inherently poor combustion characteristics [8]. It is also of note that combustion of ammonia can result in the formation of nitrogen oxides (NO_x), including NO, N_2O, and NO_2, all of which are detrimental to human health [9]. Nitrous oxide (N_2O) is also a significant greenhouse gas with a global warming potential (GWP) that is approximately 273 times greater than that of carbon dioxide (CO_2) over a 100-year period [10]. Managing NO_x emissions is henceforth critical to mitigate their adverse effects on climate and public health.

Understanding of nitrogen oxides (NO_x, N_2O) production mechanisms constitutes a fundamental requirement for the design and optimization of modern combustion systems. Extensive research has identified multiple nitrogen oxide formation pathways, leading to the establishment of various classifications within the combustion literature. The primary submechanisms recognized by the combustion community encompass the

*Corresponding author: CERFACS, 42 avenue Gaspard Coriolis, 31057 Toulouse, France
Email address: vargas@cerfacs.fr (Héctor J. Vargas Ruiz)

thermal NO route (Zeldovich mechanism) [11], the prompt NO route (Fenimore mechanism) [12], the NNH route [13, 14] and the N_2O route [15]. Additional submechanisms documented in the literature may have significant influence on NO production especially in ammonia-hydrogen combustion systems. The fuel NO submechanism describes the pathway through which nitrogen oxides are generated directly from the oxidation of nitrogen-containing fuels and was initially characterized in coal combustion processes [16, 17]. In ammonia flames, however, the fuel NO submechanism refers to distinct chemical reaction pathways, primarily comprising the HNO route [18] and the NH_i pathway [19]. In certain circumstances, like low-temperature regions near cold walls, $NO \rightleftharpoons NO_2$ interconversion reactions consume NO [20, 21]. Further submechanisms involve hydrogen-containing complex radicals, including H_2NO, which exhibits predominant activity at low temperatures [22], and HNNO which demonstrates enhanced activity under elevated pressure conditions [23]. Finally, the so-called thermal deNO_x mechanism (reburn mechanism) is a reduction process where NO is converted back into molecular nitrogen (N_2) and water, typically through reactions with ammonia-derived radicals like NH_2. This pathway is particularly important in ammonia-rich flames, acting as a natural mitigating process to reduce NO emissions. It is most effective in environments with excess ammonia or ammonia radicals. Each mechanism is dependent on specific flame conditions such as temperature, fuel composition, and oxygen availability, making it fundamental to consider all these factors when identifying NO production for combustion system design.

In an effort to find a high-performance burner design with low emissions, various burner configurations have been developed [24, 25, 26], with particular interest in systems featuring stratified fuel injection as they can replicate the heterogeneous mixing conditions found in practical gas turbine applications. The burner considered for the present investigation is the Cardiff burner with differentiated fuel injection [25, 27, 28, 29]. In this injection mode, one fuel is injected separately from the other, creating a stratified heterogeneous mixture where the fuel composition varies spatially throughout the combustion zone. This burner configuration thus enables the study of interactions between fuels of varying properties, such as ammonia's slow-burning nature and hydrogen's high reactivity and diffusivity. In the present case, the primary fuel, ammonia, is premixed with air while hydrogen is injected separately through six injection holes located 4 cm upstream of the injector's burner lip. This configuration has been experimentally investigated in previous work [25, 30, 31]. Previous numerical work [32] on this configuration revealed local variations in equivalence ratio and fuel composition as well as influence of differential diffusion effects thus presenting significant challenges for accurate modeling and simulation. However, that study focused primarily on the implementation and validation of the Multi-Fuel Thickened Flame LES (MF-TFLES) turbulent combustion model and its impact on flame topology, while NO formation mechanisms and concentrations were not thoroughly investigated. The present work addresses this gap by providing a detailed analysis of NO_x formation pathways and emissions.

Previous numerical studies of multi-fuel systems have employed various modeling approaches to capture the complex interactions in differentiated fuel injection configurations. Among these approaches, the MF-TFLES model has been specifically formulated to take into account flames with differentiated fuel injection and capture the

resulting effect of spatially evolving fuel compositions, while also dealing with differential diffusion effects. Indeed, the MF-TFLES model relies on a transported mixture fraction to track the spatial evolution of each fuel stream, thereby accounting for local variations in equivalence ratio and fuel composition. This strategy has been successfully applied in ammonia-hydrogen swirled flames [32], hydrogen-air explosions [33], and stratified hydrogen-air mixtures [34, 35].

While the MF-TFLES model successfully captures flame structure and dynamics, detailed analysis of pollutant formation requires additional chemical modeling capabilities. To investigate the specific pathways of nitrogen oxides formation, the present study employs an analytically reduced chemistry (ARC) [36] using finite rate chemistry that enables a comprehensive Cell-by-Cell (CBC) analysis of nitrogen oxide formation [37]. This methodology provides a spatial resolution of chemical reaction rates as well as species concentrations, allowing for a detailed quantification of individual reaction contributions to NO production. Through this approach, the dominant mechanisms governing nitrogen oxide formation in ammonia-hydrogen swirled flames under various operating conditions can be systematically identified and characterized, providing a better understanding of the complex interplay between fluid dynamics, mixing, and chemical kinetics in these multi-fuel combustion systems.

The present investigation demonstrates that the HNO route dominates NO formation across all equivalence ratios studied (ϕ = 0.65 to 1.2), contributing approximately 90% of total NO production, while other pathways remain limited. Additionally, the study shows that NO emissions are highly sensitive to equivalence ratio variations, with peak emissions occurring at ϕ = 0.8 despite higher formation rates at leaner conditions due to effective reburn mechanisms.

The paper is organized as follows: first, Section 2 presents the experimental and numerical setups studied; next, in Section 3, the experimental results including chemiluminescence and PLIF data are used to validate the LES predictions. Then, the NO sub-mechanisms are analyzed by use of the proposed CBC methodology.

2. Setup and methodology

2.1. Experimental setup and methodology

The tangential swirl burner first introduced by Mashruk *et al.* [25] is employed for this investigation. The primary fuel, ammonia, is premixed with air while hydrogen is injected separately through six injection holes located 4 cm upstream of the injector's burner lip. Ten operating points, detailed in Table 1, were examined experimentally. A 70/30 NH_3/H_2 blend (by volume) at 20 kW thermal power for equivalence ratios from ϕ = 0.65 to 1.6 was probed. All conditions were maintained at atmospheric pressure ($\sim$ 1.1 bar) and ambient temperature ($\sim$ 288K). The complete experimental dataset can be found in supplementary material. Reactants were supplied through high-precision Bronkhorst EL-FLOW Prestige mass flow controllers (MFCs) operated with flows within 15 – 95% of the full mass flow range capabilities with an accuracy of $\pm$0.5%, as documented in [25]. The system includes dedicated supply lines for NH_3, H_2, N_2 (dilution), along with a dry air compressor. Eight K-type thermocouples (3 mm diameter) were strategically positioned to characterize the temperature profile of the

Table 1: Test points investigated experimentally.

Test Point	TP01	TP02	TP03	TP04	TP05
ϕ	0.65	0.7	0.8	0.9	1.0
Test Point	TP06	TP07	TP08	TP09	TP10
ϕ	1.1	1.2	1.3	1.4	1.6
Fuel: $X_{NH_3} = 0.7$, $X_{H_2} = 0.3$			Power: 20 kW		

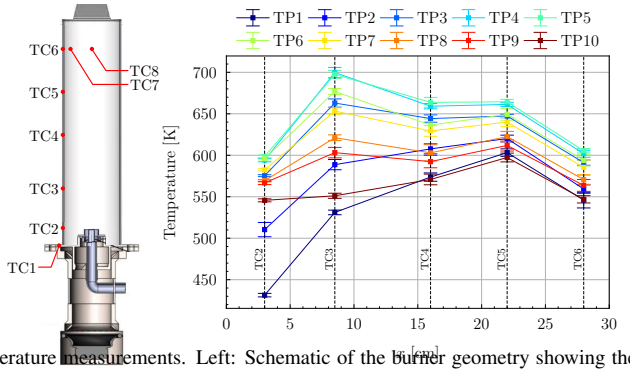

Figure 1: Temperature measurements. Left: Schematic of the burner geometry showing thermocouple positions. Right: Temperature profiles measured along the quartz tube length for operating points TP1-TP10. The x-coordinate represents the axial distance from the burner backplate.

quartz tube (Fig. 1). Thermocouple 1 (TC1) was placed at the outer wall of the backplane. Thermocouples 2 – 6 (TC2-TC6) were positioned along the outer wall of quartz tube at $x = [3, 8.5, 16, 22, 28]$ cm. Thermocouple 7 (TC7) was located 4 cm from quartz exit and 1 cm from the quartz tube inner wall, while thermocouple 8 (TC8) measured the centerline flame temperature 4 cm from quartz exit. Data acquisition was performed using a TC-08 Thermocouple Data Logger at 10 Hz frequency. Measurements were averaged over 120 per condition. Pre-experimental calibration showed a maximum difference of ±2 degrees between thermocouples. Temperature measurements were corrected for convective and radiative heat transfer effects using the expression proposed in [38].

The setup employed two Lavision Image Intense CCD cameras with dedicated Intensified Relay Optics (IRO) image intensifiers, operating simultaneously at 10 Hz with 80% gain. Species-specific Edmund optical filters were used to detect OH* (309 nm; $A^2\Sigma^+ - X^2\Pi$ system) [39], NH* (336 nm; $A^3\Pi - X^2\Sigma^-$ system) [39, 40, 41, 42], and NH_2* (630 nm; single peak of the NH_2 α band) [39, 43]. LaVision DaVis 11 software was used to collect 300 frames per condition. Image processing included a 3×3 pixel gaussian filter, background removal, temporal averaging, followed by Abel deconvolution of the post-processed images using the Hansen-Law algorithm [44].

The NO-PLIF measurements were performed using the setup illustrated in Fig. 2. The laser excitation was provided by a Continuum Powerlite^{TM} Precision II Nd:YAG laser operated at its third harmonic (355 nm), delivering 320 mJ per pulse at 10 Hz. This pump laser was coupled to a Sirah Cobra-Stretch dye laser system utilizing Coumarin 2 (also known as Coumarin 450) dye solution. The dye laser output, centered at 473 nm, was frequency-doubled through the integrated frequency conversion unit (FCU). The resulting beam was directed through a series of four Pellin-Broca prisms to generate the

desired excitation wavelength of 236.5 nm with an output energy of 5.5 mJ. Shot-to-shot variations in laser energy were monitored and recorded using the LaVision DaVis 11 system. For each operating condition, 200 instantaneous images were acquired.

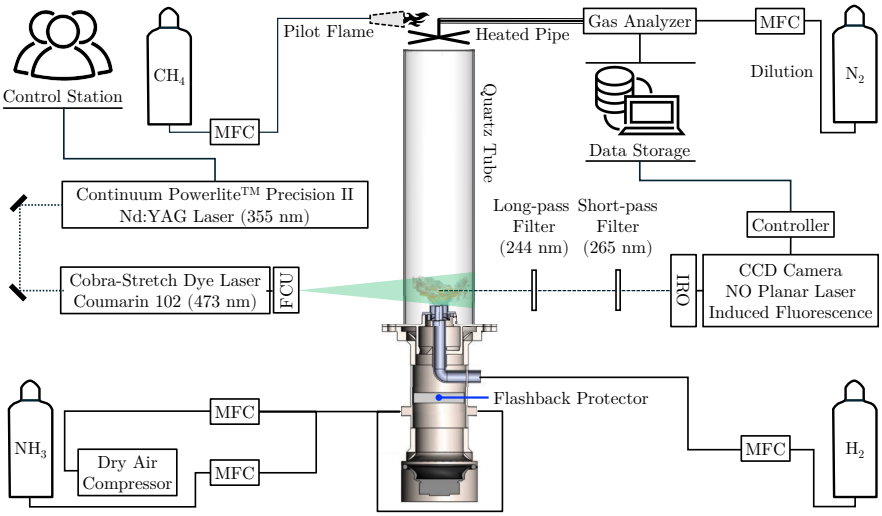

Figure 2: Schematic representation of the experimental setup showing the burner assembly, flow control systems, and diagnostic equipment.

The fluorescence signal was captured using a LaVision M-lite 2*M* camera coupled with a dedicated IRO X image intensifier operating at 75% gain. The system was configured to excite NO molecules at 235.875 nm (online measurement), with offline measurements conducted at 235.842 nm to account for background interference (Fig. 3a). The fluorescence signal from NO $(0-1)$ transition was collected in the $245-270$ nm spectral range, with scattered light suppression achieved through the combination of a 244 nm long-pass filter (Filter A, Semrock - LP02-244RS-50.8-D) and a 265 nm short-pass filter (Filter B, Asahi Spectra - ZUS0265), as per [45]. The detectable wavelength range is shaded in gray. The fluorescence signal contributions of NO A−X $(0-1)$ in the range $240-300$ nm simulated using the LIFBASE tool [46] as well as the transmittance behavior of the filters are shown in Fig. 3b. Finally, flame visualization was performed using a Hasselblad camera equipped with an OmniVision OV64B sensor. The camera was positioned perpendicular to the quartz tube at 2 meters distance and was operated at 70 mm equivalent focal length with $f/2.6$ aperture. Data were recorded at 60 Hz frame rate for 10 seconds per test point, maintaining constant gain settings across all operating conditions to ensure consistent light sensitivity.

2.2. Numerical setup and methodology

Starting from the numerical domain described in our previous work [32], a Static Flame Refinement (SMR) approach allowed to obtain a 41 million cell unstructured tetrahedral mesh. For this refinement process, the time-averaged HRR field resulting from the TP01 simulation was used to identify the reactive region (RR) downstream of

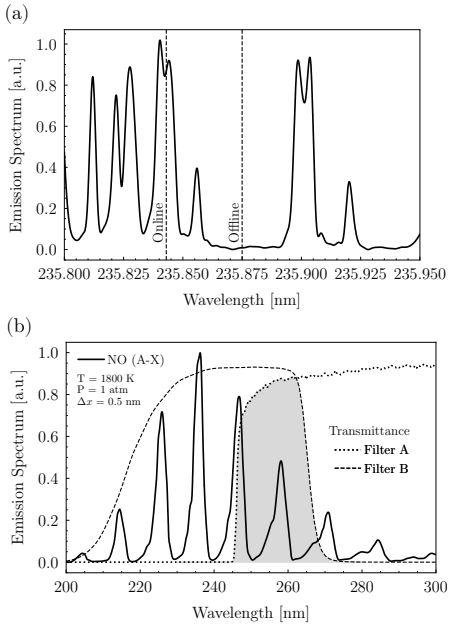

Figure 3: (a) NO (A−X) emission spectrum overlaid with the transmission curves of the optical filters: Semrock LP02-244RS (Filter A), the ZUS0265 UV (Filter B). (b) NO fluorescence scan showing the average signal detected. Arbitraty units (a.u.) are used.

the burner nozzle where HRR $\geq 0.1\%\text{HRR}_{\text{max}}$ and for which the element size was set to be constant so that $\Delta x_{\text{RR}} = 800\ \mu$m as displayed in Fig. 4. Note that the injection and mixing regions upstream of the reactive zone did not require any further refinement. To ensure temporal convergence, the following procedure was adopted: 20 ms of reactive simulation using a mesh previously validated for accurate flow description [32] and flame stabilization, followed by 60 ms on the refined SMR mesh to achieve adequate flame resolution and thermal convergence, and a final 60 ms of statistically converged reactive flow from which the fields presented in this paper were extracted. The numerical simulations presented in this paper were conducted using AVBP[1] [47], a parallel explicit cell-vertex code developed at CERFACS. The selected numerical scheme is the second-order accurate Lax-Wendroff scheme [48]. For turbulence modeling, the Sigma closure [49] is selected to close the sub-grid Reynolds stresses because of its proven reliability in swirling flow configurations. The NSCBC formalism [50] is enforced at the inlet and outlet boundary conditions, while walls which are not in contact with the reactive region are treated as no-slip adiabatic surfaces.

Since the main objective of the present study is to characterize NO formation, heat losses, which are know to be of importance, are addressed through the use of a Heat Resistivity Tuning (HRT) approach [51]. This method is chosen to account for the thermal resistances and heat transfer effects within the system, ensuring that the simulation

[1] http://www.cerfacs.fr/avbp7x

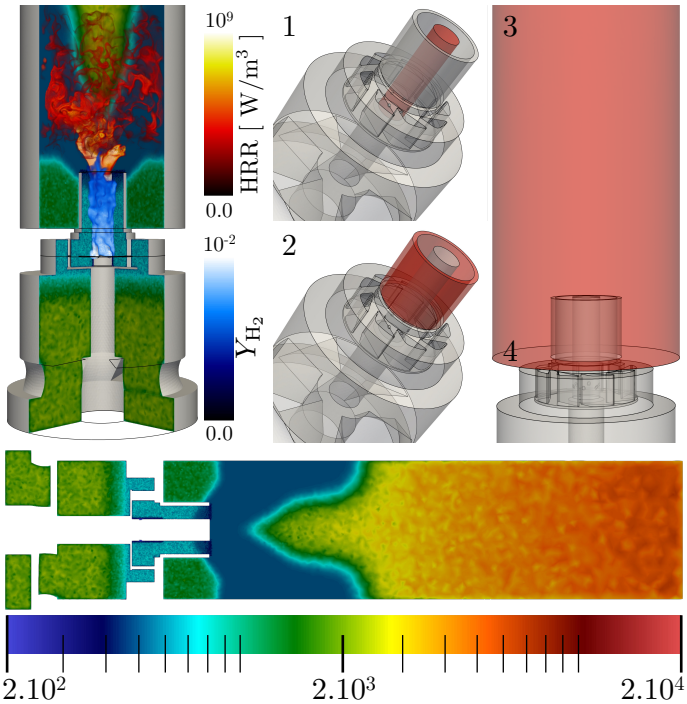

Figure 4: Computational domain. Left: Instantaneous field showing Heat Release Rate (HRR) and H_2 mass fraction. Right: Heat loss surfaces are highlighted shown in red: (1) central rod, (2) injector nozzle ring (3) quartz tube and (4) burner backplate. Bottom: Mesh size distribution.

accurately reflects the thermal losses inherent to such systems and reflects its impact on the combustion process.

Note that walls in contact with the reactive region require special consideration due to significant heat transfer effects. For the simulations, heat losses are prescribed for four key surfaces of the geometry, shown in red in Fig. 4: (1) the injector central rod, (2) the injector ring, (3) the quartz tube, and (4) the backplane. The heat loss estimation process involved comparing inlet and exhaust gas enthalpies at equilibrium using available experimental data. For all surfaces with prescribed heat losses (HL_{wall}), the normal heat flux per unit area ($\dot{q}_{wall}$) follows,

$$\dot{q}_{wall} = \frac{-(T_{wall} - T_{ref})}{R_{wall}}, \tag{1}$$

where T_{ref} represents the reference (or target) temperature and R_{wall} is the heat resistance. The heat resistance values are set to the value found in our previous work [32] and are maintained in this study: $R_{injec} = 6.93 \cdot 10^{-4}$ K.m^2.W^{-1} for the injector lips and $R_{comb} = 2.0 \cdot 10^{-2}$ K.m^2.W^{-1} for the combustor. For the quartz wall, detailed axial temperature profiles were reconstructed from experimental measurements using Bezier curve approximations. These profiles are presented in supplementary material and are applied hereafter for all simulations.

The turbulent combustion modeling approach selected couples the MF-TFLES model [32], which makes use of two passive mixture fraction scalars integrated with the NH3H2N2_15_211_5_HV ARC itself encompassing 15 transported species, 211 unitary reactions and 5 Quasi-Steasy-State (QSS) species. To account for the SGS flame-turbulence interaction and the loss in wrinkling due to the thickening of the flame, the efficiency function developed by Charlette et al. [52] is used. A specialized relaxation flame sensor [53], developed for reactive LES simulations with ARC schemes, enables the flame front detection.

Correct numerical discretization of the reactive front is ensured by thickening the flame up to a prescribed seven-point resolution. The modeling also implements a modified Takeno flame index [54] variant introduced by Cellier [55], computing species-specific flame indices for NH_3 and H_2. Transport phenomena are modeled using a mixture-averaged approach. The passive scalar transport properties are modeled in a similar fashion so as to ensure consistency.

2.3. NO sub-mechanism identification methodology

The identification and quantification of nitrogen oxide formation pathways follows the CBC methodology first used by Rouland et al. [37] as well as the pathway classification established by Yan et al. [19]. This classification was adapted and extended for the NH3H2N2_15_211_5_HV (ARC) developed in our previous work [32]. Through such an approach, a systematic classification of chemical reactions contributing to NO production or consumption, based on their roles and kinetic pathways, is possible. The sub-mechanisms are classified into three distinct types: *direct* reactions that directly produce or consume NO, *activation* reactions that generate reactive intermediates and *interconversion* reactions that facilitate the transformation between nitrogen-containing species.

Table 2 presents the comprehensive classification of NO sub-mechanisms identified within the reduced chemical mechanism, categorizing each pathway according to its type and listing the primary contributing reactions. Note that all main reactions identified by Yan et al. [19] are contained within the used ARC chemistry, confirming the capability of the reduced mechanism to correctly retrieve all contributions like the reference detailed mechanism counterpart would (being limited only by the accuracy of the detailed mechanism itself).

The thermal sub-mechanism encompasses the classical Zeldovich reactions involving atomic nitrogen, while the thermal DeNO$_x$ pathway represents the reverse consumption of NO through interactions with NH_2 and NH radicals. The HNO route constitutes a significant pathway in ammonia combustion, involving multiple reactions that both produce and consume NO through HNO intermediates. The N_2O pathway includes both direct NO formation through N_2O decomposition and the activation of N_2O itself. Additional pathways involving NH_i radicals, NO_2 species, H_2NO species, and NNH species contribute to the overall nitrogen oxide chemistry, with some reactions serving dual roles in both NO formation and consumption processes.

This comprehensive framework enables a detailed analysis of NO production and consumption rates within each computational cell, facilitating the identification of dominant pathways under varying flame conditions and equivalence ratios.

Table 2: Chemical sub-mechanisms and their main reactions involved in NO formation and consumption pathways as identified by Yan *et al.* [19] and extended in the present study, considering the NH3H2N2_15_211_5_HV ARC mechanism from our previous work [32].

Sub-Mechanism	**Type**	**Contributing Reactions**
Thermal	Direct	$N + NO \rightleftharpoons N_2 + O$
		$N + OH \rightleftharpoons H + NO$
		$N + O_2 \rightleftharpoons NO + O$
Thermal $DeNO_x$	Direct	$NH_2 + NO \rightleftharpoons NNH + OH$
		$NH_2 + NO \rightleftharpoons H_2O + N_2$
		$NH + NO \rightleftharpoons H + N_2O$
HNO	Direct	$H + HNO \rightleftharpoons H_2 + NO$
		$HNO + O \rightleftharpoons NO + OH$
		$HNO + OH \rightleftharpoons H_2O + NO$
		$HNO + O_2 \rightleftharpoons HO_2 + NO$
		$HNO + NH_2 \rightleftharpoons NH_3 + NO$
		$HNO \rightleftharpoons H + NO$
		$HNO + N_2 \rightleftharpoons NNH + NO$
N_2O	Direct	$N_2O + OH \rightleftharpoons HNO + NO$
		$N_2O + O \rightleftharpoons 2NO$
N_2O	Activation	$N_2O(+M) \rightleftharpoons N_2 + O(+M)$
NH_i	Direct	$NH + O_2 \rightleftharpoons NO + OH$
		$NH + O \rightleftharpoons H + NO$
		$NH + NO \rightleftharpoons N_2 + OH$
H_2NO	Direct	$NH_2 + NO_2 \rightleftharpoons H_2NO + NO$
NNH	Direct	$NNH + O \rightleftharpoons NH + NO$
NNH	Activation	$NNH \rightleftharpoons H + N_2$
		$H + NNH \rightleftharpoons H_2 + N_2$
$NNH \rightleftharpoons N_2O$	Interconversion	$NNH + O \rightleftharpoons H + N_2O$
$NNH \rightleftharpoons N_2$	Interconversion	$NNH + O \rightleftharpoons N_2 + OH$
		$NNH + O_2 \rightleftharpoons HO_2 + N_2$
NO_2	Direct	$NO_2 + OH \rightleftharpoons HO_2 + NO$
		$NO_2 + O \rightleftharpoons NO + O_2$
		$2NO_2 \rightleftharpoons 2NO + O_2$
		$NO_2 + N_2 \rightleftharpoons NO + N_2O$
		$NO_2(+M) \rightleftharpoons NO + O(+M)$

3. Results and discussion

From the experimental points presented in Table 1, four specific operating points were selected for numerical simulations: TP01 (ϕ = 0.65), TP03 (ϕ = 0.8), TP05 (ϕ = 1.0), and TP07 (ϕ = 1.2). The numerically obtained flames are analyzed and discussed in Section 3.1 and Section 3.2. Subsequently, Section 3.3 discusses the equivalence ratio effect on the flame shape. Once the flame stabilization and geometry have been discussed and validated, resulting pollutant emissions are investigated in Section 3.4.

3.1. Flame shapes

The experimental time-averaged flames are presented in Fig. 5. For the leanest case (TP01), the flame exhibits blue emissions near the flame base indicative of H_2-dominated combustion while stoichiometric and rich conditions (TP05, TP07) display uniform orange emission characteristic of NH_3 combustion throughout the flame.

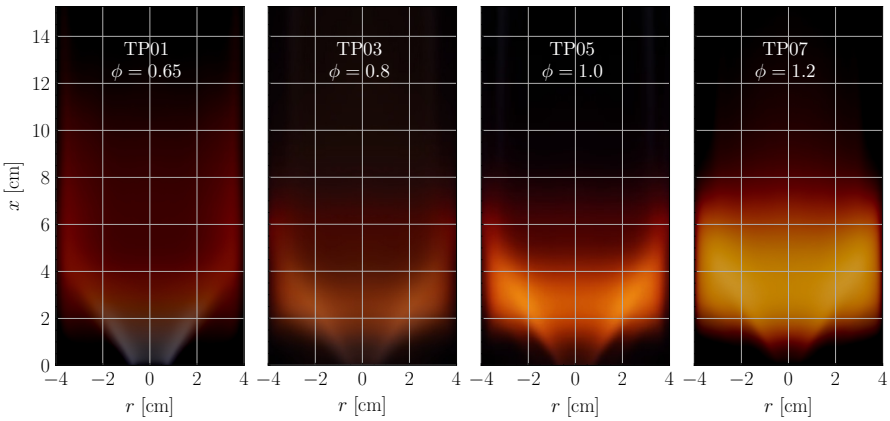

Figure 5: Experimentally obtained time-averaged visible flame luminosity for the 70/30 NH_3/H_2 mixture at 20 kW under varying equivalence ratios.

The validation of numerical predictions against experimental measurements is presented in Fig. 6 and Fig. 7, comparing the filtered heat release rate (HRR $* \mathcal{F}$) with OH* chemiluminescence signals. The numerical HRR is multiplied by the thickening factor $\mathcal{F}$ since it varies both spatially and temporally within each flame and among different flames. This normalization by $\mathcal{F}$ also ensures a proper comparison of HRR distributions across all operating conditions. Both HRR $* \mathcal{F}$ and OH* fields are then self-normalized to allow a comparison of the flame structures. At very lean conditions (TP01), the flame tail length after the high-intensity flame foot is slightly underestimated by the numerical simulation although the flame angle is in correct agreement with the experimental results. Note that, while the normalized fields suggest a compact V-shape flame structure, the actual flame extends further downstream both experimentally and in LES. The intense signal concentration at x = 0.5 cm mainly located at the burner exit was identified as resulting from preferential diffusion effects with H_2 accumulating at the flame base. This creates a highly reactive zone near the injection point which overshadows the weaker downstream flame regions through the re-normalization.

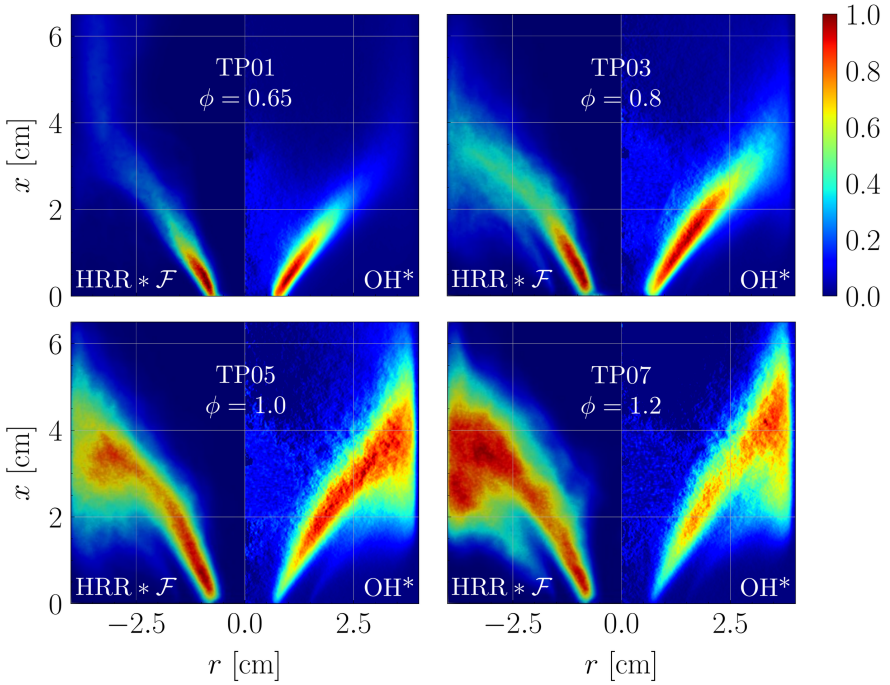

Figure 6: Self-normalized numerical heat release rate (HRR$*\mathcal{F}$, left half) and experimental OH* chemiluminescence (right half).

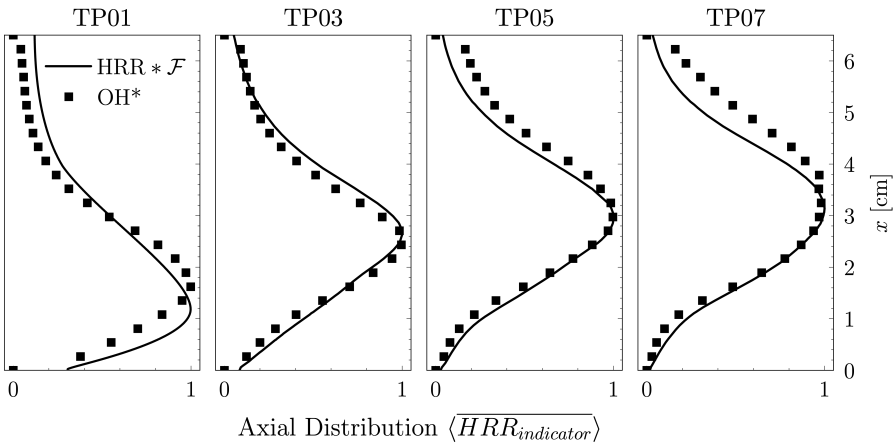

Figure 7: Axial average resulting from the radial integral of numerical and experimental HRR markers.

This interpretation is supported by flame visualization data (Fig. 5), showing a blue flame base characteristic of H_2 combustion transitioning to an orange flame tip typical of NH_3 combustion. In contrast, the stoichiometric flame (TP05) exhibits a uniformly orange emission map throughout the flame length.

As the equivalence ratio increases to $\phi = 0.8$ (TP03), the flame branches extend to $x = 4$ cm while maintaining their anchoring position. For this test point, the high

intensity region is contained in the 0 cm $< x <$ 1.8 cm axial range in the LES, while its experimental counterpart extends from the burner nozzle tip to $x = 2.2$ cm.

For TP05, *i.e.* at stoichiometric conditions, the flame exhibits a larger opening angle, with comparable values between the numerical prediction and the experiment (~45°). The flame branches extend to $x = 6$ cm with an intensity maximum around $x = 3.5$ cm and a radial spread which reaches the quartz wall at $r = 4$ cm. Both experimental OH* signal and numerical HRR $*\mathcal{F}$ show consistent spatial distributions. Finally, going to TP07 ($\phi = 1.2$), the flame angle is again correctly predicted although the axial maximum appears at $x = 3.5$ cm when the experimental maximum position is identified to be around $x = 4.2$ cm.

Figure 8 presents the NO distribution fields obtained numerically and experimentally by use of NO-PLIF, confirming the good agreement between predictions and measurements across all equivalence ratios. For lean conditions, NO is primarily found in the Central Recirculation Zone (CRZ).

For TP01 (Fig. 8 - first column), particularly high concentrations of NO arise in the adjacent downstream region of the reactive front, with instantaneous fields showing distinct high-intensity regions near the main flame front. As ϕ increases to 0.8 (TP03), the high intensity region is more evenly distributed, throughout the CRZ zone, for both numerical and experimental results. At stoichiometric conditions (TP05), both instantaneous and averaged fields indicate more distributed NO concentrations.

Note that the NO concentration in the Outer Recirculation Zone (ORZ) is identifiable under lean and stoichiometric conditions, with its intensity (relative to the CRZ) increasing from TP01 to TP05, for which the ORZ and CRZ intensities of NO become comparable. Under rich conditions (TP07), NO is primarily found along the high-temperature reactive front, as observed in both instantaneous and time-averaged fields.

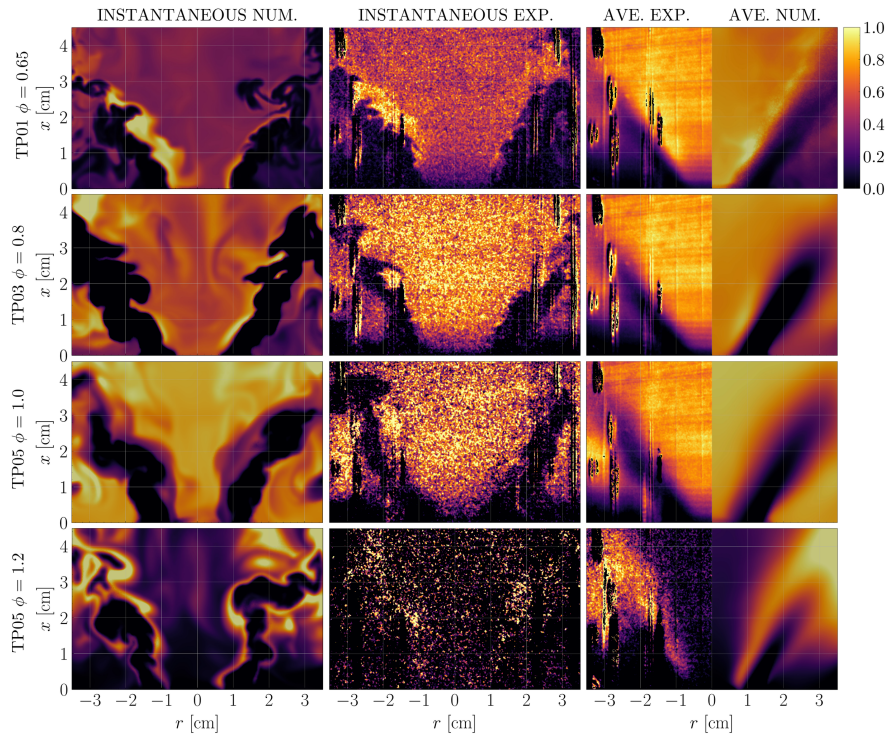

Figure 8: Comparison between numerical NO mass fraction fields and experimental NO-PLIF measurements. Left column: instantaneous NO mass fraction from LES. Middle column: instantaneous NO-PLIF signal. Right column: time-averaged experimental NO-PLIF (left half) and numerical NO mass fraction (right half). All fields are self-normalized.

3.2. Adiabaticity analysis

As indicated above, a critical element of proper NO formation prediction stems from the adequate evaluation of naturally present heat losses of any experimental or real burner. The analysis of heat losses in combustion systems however usually goes through the quantification of what is referred to as the non-adiabatic degree in the burner. To do so, one usually relies on the adiabaticity parameter η, defined as:

$$\eta = \frac{T_{HL}^{equil} - T_{ref}}{T_{adb}^{equil} - T_{ref}}, \tag{2}$$

where T_{HL}^{equil} is the equilibrium temperature accounting for heat losses, T_{adb}^{equil} is the adiabatic equilibrium temperature and T_{ref} is the reference fresh gas temperature (288 K). The fresh gas temperature is the injection temperature for both the H_2 stream and the NH_3-Air stream. This parameter ranges from 0 to 1, with $\eta = 1$ indicating adiabatic conditions and $\eta = 0$ corresponding to maximum heat loss.

In the above expression, the equilibrium temperatures are computed at constant pressure using the local thermodynamic state. The temperature T_{HL}^{equil} is determined

using local temperature and the local ARC species mass fractions, while T_{adb}^{equil} is computed by reconstructing the corresponding reference fresh gas state (288 K, 1.1 bar) using the local concentration of the transported passive scalars of the MF-TFLES turbulent combustion model.

The analysis of the adiabaticity field involves time-averaging over 60 ms of the statistically converged turbulent flow. The three-dimensional data is then processed through azimuthal averaging using 360 equi-distributed planes (one degree intervals), generating the half-domain representation shown in Fig. 9.

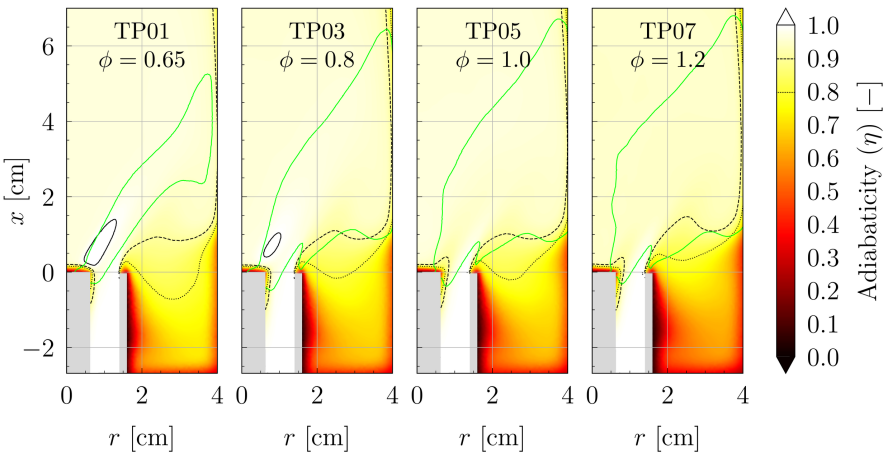

Figure 9: Adiabaticity field. The reactive front is identified through the green isoline set to 5% max(HRR$*\mathcal{F}$). Black lines show adiabaticity isocontours at 1.0 (solid), 0.9 (dashed) and 0.8 (dotted).

The visualization of adiabaticity fields indicates the level and location of the non-adiabatic degree across the four operating conditions. For all cases, there are no heat losses well upstream of the injector tip, as the local temperature equals T_{ref}. Near the tip of the central rod, however, heat losses occur due to the flame being nearby. Therefore, this region of the flow constitutes the preheating zone of the inner flame branch (IB), which has a temperature higher than T_{wall}^{ref} from the HRT methodology, resulting in heat losses in that zone. This is illustrated by the $\eta = 0.9$ near the central rod tip isoline, which is visible in all cases.

For TP01, a super-adiabatic region ($\eta > 1$) appears near the central rod of the nozzle, attributed to preferential diffusion of hydrogen in lean flames. This effect diminishes at higher equivalence ratios, becoming less pronounced for TP03 and disappearing for TP05 and TP07, corroborating prior flame visualizations (Fig. 5).

The IB predominantly exists in regions where $\eta > 0.9$ (dashed black lines), the reactive region (green contour) remaining within the $\eta > 0.8$ envelope. Note that lower adiabaticity ($\eta < 0.8$) near the nozzle ring, creates a cold *gap* between the flame and ring surface, reducing the flame intensity of the outer branch across all operating conditions. Strong heat-losses are observed near the back plate, this is expected as the reference temperature in that region is lower leading to a greater heat flux through the steel experimental installation when compared to that of the quartz tube.

Note also that the observed degree of adiabaticity supports the use of the adiabatic flame assumption used to built the reference look-up table for the turbulent combustion model. Furthermore, the naturally thick nature of ammonia-rich flames, such as the ones found in the outer branch of the flame, reduces the impact of local heat losses on the thickening factor computation. However, the observed deviations from perfect adiabaticity are likely to influence pollutant formation, particularly near walls and in the post-flame region. This effect is investigated in the following sections.

3.3. Equivalence ratio impact on flame shape

Once the flames have been presented via experimental data and simulations, it is possible to further analyze the impact of equivalence ratio on the flame shape. The normalized distributions of $\langle\overline{\dot{\omega}_T * \mathcal{F}}\rangle$ for cases TP01, TP03, TP05 and TP07 are presented in Fig. 10a. The fields are colored following the logarithmic expression $\log_{10}\left[(\dot{\omega}_T * \mathcal{F}) \ / \ (\max_{i\in\text{cases}}(\dot{\omega}_T * \mathcal{F})_i)\right]$ for better visualization.

To obtain a more quantitative comparison between all flames in terms of shape and stabilization, the time-averaged heat release rate is integrated over the combustor cross section S to obtain the one-dimensional mean axial distribution $\langle\overline{\dot{\omega}_T * \mathcal{F}}\rangle(x)$:

$$\langle\overline{\dot{\omega}_T * \mathcal{F}}\rangle(x) = \frac{1}{S}\iint_S \overline{\dot{\omega}_T * \mathcal{F}}(x, y, z)dydz. \tag{3}$$

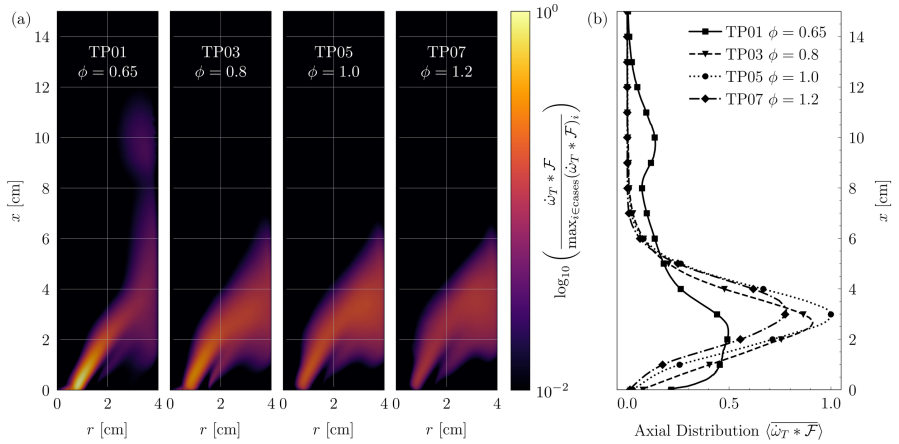

Figure 10: (a) Time-averaged heat release rate distribution in the azimuthally-averaged longitudinal half-section for the 70/30 NH_3/H_2 mixture at 20 kW, normalized by its maximum value and plotted in logarithmic scale. (b) Corresponding mean axial distributions of the heat release rate averaged over cylindrical sections.

Thanks to such an integrated view, two main behaviors are observed, a downstream shift of the peak intensity from lean to rich conditions and a particularly high IB intensity in lean cases. Indeed, under lean conditions, the already observed effect of preferential diffusion causes hydrogen to concentrate at the flame's IB base, resulting in localized high-intensity regions. The IB intensity progressively decreases with increasing equivalence ratio, while the outer branch shows the opposite trend, becoming more prominent in rich conditions.

Figure 10b shows the axial distribution of the normalized numerical values $\langle\overline{\dot{\omega}_T * \mathcal{F}}\rangle$, taking the central rod tip as the coordinate origin ($x = 0$ cm). The stoichiometric flame (TP05) exhibits the highest overall intensity, with its peak at $x = 2.97$ cm serving as the reference value. Under moderately lean conditions (TP03), the peak occurs slightly upstream at $x = 2.66$ cm, reaching 91% of the global maximum. The rich flame (TP07) shows more evenly distributed heat release intensity, with its maximum located furthest downstream at $x = 3.14$ cm, achieving 80% of the global maximum intensity and maintaining significant heat release up to $x = 6$ cm.

The leanest case (TP01) presents two peaks of decreasing intensity along the axial direction: a primary region of elevated heat release extending from $x = 0.84$ cm to $x = 2.26$ cm with 49% of the global maximum intensity, and a secondary peak at $x = 9.72$ cm reaching 14% of the global maximum. This distribution results from the combination of intense reactions in the hydrogen-enriched flame base and sustained combustion in the outer flame branch, which *unfolds* downstream of the main reactive region.

3.4. NO Sub-mechanism identification

The spatial distributions of nitrogen oxide species (NO, NO_2, N_2O) are investigated in this section. To do so, the solutions were averaged over 60 ms of statistically converged unsteady results and the fields displayed in the following figures are also azimuthally averaged over 360 slices. The flame location is identified through the use of the progress variable isocontour $c = 0.85$, where c is locally defined as:

$$c(\mathbf{x}, t) = \frac{Y_c(\mathbf{x}, t) - Y_c^u(\mathbf{x}, t)}{Y_c^b(\mathbf{x}, t) - Y_c^u(\mathbf{x}, t)}, \tag{4}$$

where the progress variable is constructed as $Y_c = Y_{H_2O} + Y_{NO} + Y_{N_2}$ and the superscripts u and b denote the unburnt and burnt states, respectively. These bounding states are locally computed to account for variations in fuel composition and equivalence ratio throughout the domain.

In previous works, the expected behavior of the NO concentration is to reach its maximum at $\phi = 0.8$ and then decrease to near zero in rich fuel conditions (around $\phi = 1.1 - 1.3$) [25, 56]. This trend is correctly reproduced by in the simulations. The NO distribution shown in Fig. 11 indeed demonstrates a strong dependence on equivalence ratio with highest concentrations occurring for lean conditions. For TP01, maximum concentrations are observed in the region near the flame foot of the IB (after the flame front). This nitric oxide is then reduced by unburnt ammonia near side walls so that the NO concentration overall diminishes as the flow advances downstream. As the equivalence ratio increases to TP03, the maximum peak concentration decreases but the global concentration is the highest among all cases. The NO produced in the flame indeed does not seem to be reduced in downstream burner section of the burner and flame as in case TP01. Although the NO concentration produced in the post-flame region is lower, its concentration does not decrease after the flame front. For the rich case, TP07, however the lowest NO concentration is achieved with a maximum NO concentration which appears near the flame brush where the temperature is the highest. Figure 12 shows the N_2O concentration. For cases TP03, TP05 and TP07, the N_2O concentration is limited to the flame brush region where it is created at low temperature

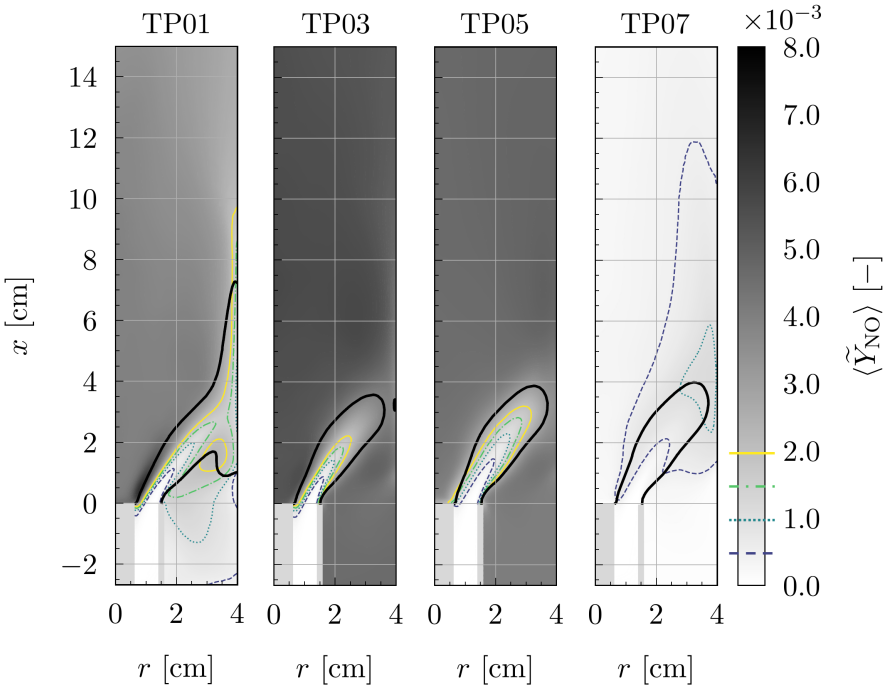

Figure 11: Time averaged NO mass fraction distributions. The solid black isolines correspond to $c = 0.85$ in each case.

and in the preheat zone of the flame to be then consumed at higher temperatures, once the flow reaches the reaction front. The behavior of TP01 however differs as N_2O is appears in the ORZ and all the way downstream near the quartz lateral wall due to the imposed heat loss which seems to quench this process. The NO_2 distribution depicted in Fig. 13 exhibits markedly different spatial characteristics compared to NO or N_2O. For the lean case, TP01, the highest concentrations occur predominantly in the ORZ and near the burner lip in the low temperature preheat zone of the flame brush. TP03 maintains a similar spatial pattern. And as the mixture approaches the stoichiometric conditions for TP05, NO_2 concentrations decrease significantly throughout the domain and become primarily confined to regions near the burner lip. The rich case TP07 then shows minimal NO_2 concentrations across most of the computational domain. Note that, NO and N_2O share similar concentration ranges of the order of 10^{-2}, while NO_2 remains approximately two orders of magnitude lower and near 10^{-4}.

The NO formation and consumption patterns are provided in Fig. 14. All cases show initial NO consumption (blue regions) followed by a production (red regions) along the progress variable gradient of the IB flame, consistent with one-dimensional flame analyses. Near-walls, NO consumption correlates with the NO-NO_2 interconversion through low-temperature reactions (reaction HO_2 + NO $\rightleftharpoons$ NO_2 + OH), as evidenced by NO_2 source term distributions (see supplementary material). Under lean conditions (TP01), high NO consumption at the IB flame foot coincides with elevated

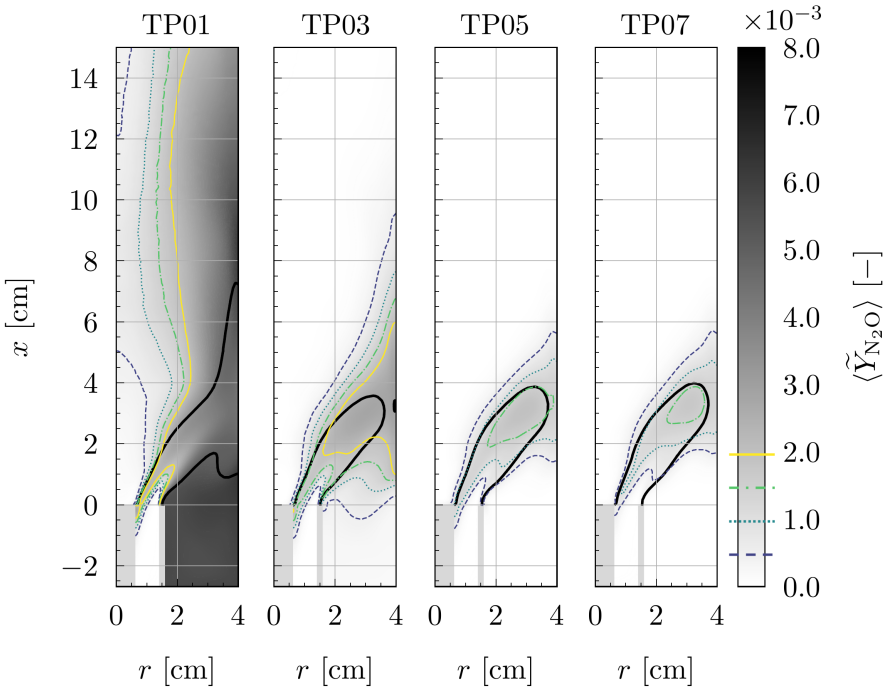

Figure 12: Time averaged N_2O mass fraction distributions. The solid black isolines correspond to $c = 0.85$ in each case.

H_2 concentrations, leading to increased temperatures and OH radical pool formation. This behavior is linked to the super-adiabatic effects observed in Fig. 9. Under moderately lean conditions (TP03), preferential diffusion of H_2 continues to influence the IB reaction zone, though less prominently than in TP01. For stoichiometric conditions (TP05), strong NO consumption appears in the CRZ, downstream of the flame front. Finally, under rich conditions (TP07), although NO consumption patterns similar to TP05 are maintained in CRZ, the intensity decreases. It is furthermore noted that the NO consumption zone extends downstream reaching the exhaust plane. The observed NO production in the outer branch may result from lower flow velocities and increased remaining fuel fraction while the post-flame region exhibits net NO consumption through thermal $DeNO_x$ and reburn mechanisms.

Regarding N_2O formation in Fig. 15, patterns follow progress variable gradients similar to NO evolution. NO consumption directly correlates with N_2O and NO_2 production in the preheat zone. This low-temperature phenomenon is particularly evident at the flame foot near walls where heat losses dominate. For cases TP03, TP05 and TP07, N_2O is consumed immediately downstream of the reactive front due to the presence of NH_i radicals. Conversely, in the leanest case (TP01) where NH_i radicals are sparser, N_2O is only consumed in the post-flame region to a lesser extent resulting in lower N_2O exhaust levels as illustrated in Fig. 12.

Figure 16 presents the volumetric contributions from the identified NO sub-mechanism across the four operating conditions,*i.e.*, TP01, TP03, TP05 and TP07. The time-averaged spatial distribution of these sub-mechanism contributions is provided in the

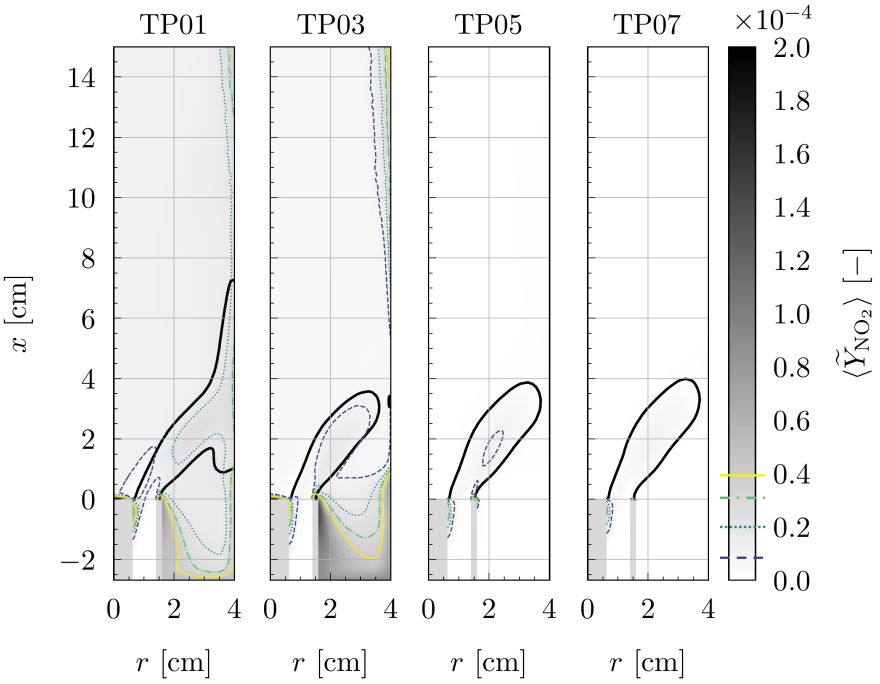

Figure 13: Time averaged NO_2 mass fraction distributions. The solid black isolines correspond to $c = 0.85$ in each case.

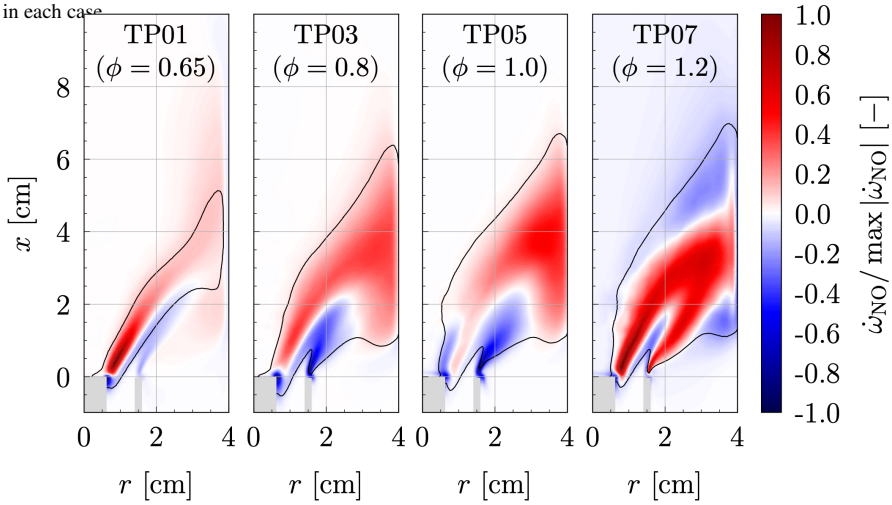

Figure 14: Time averaged self-normalized NO source term. The reactive front is identified through the black isoline set to 5% max(HRR $* \mathcal{F}$).

supplementary material. The analysis quantifies the integrated production rate of these pathways using the volume-weighted reaction rate:

$$\int_V \dot{\omega}_{NO}^{\text{sub-mech}} dV, \tag{5}$$

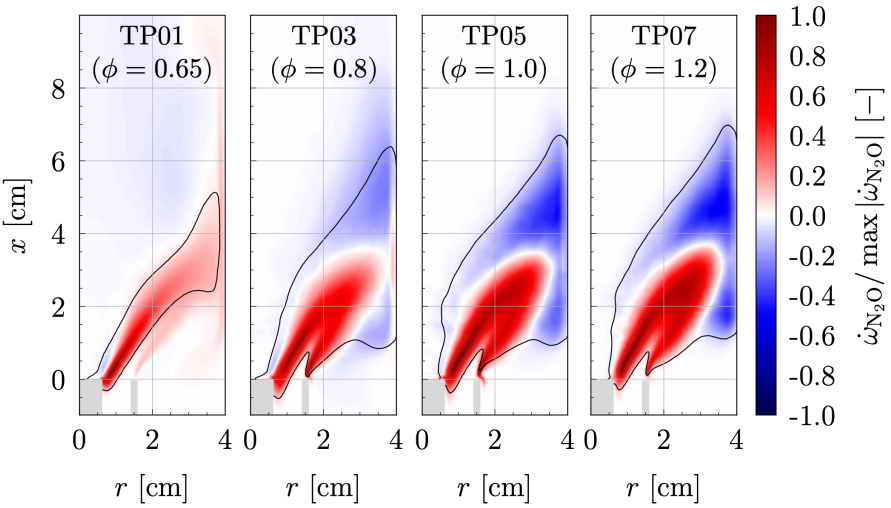

Figure 15: Time averaged self-normalized N_2O source term. The reactive front is identified through the black isoline set to 5% max(HRR $* \mathcal{F}$).

where $\dot{\omega}_{NO}^{\text{sub-mech}}$ represents the net NO production rate for a sub-mechanism. The integration is performed over the entire computational domain volume V. The sum of integrated sub-mechanism contributions are in excellent agreement with the total NO source term integral ($\int_V \dot{\omega}_{NO}\, dV$), with relative errors ranging from 1.23% to 3.00% across all test points. Among production mechanisms (thermal, N_2O, HNO, H_2NO, NO_2 and NH_i), the HNO route is clearly the dominant contributor across all operating conditions, confirming what had been reported in the literature [18]. This sub-

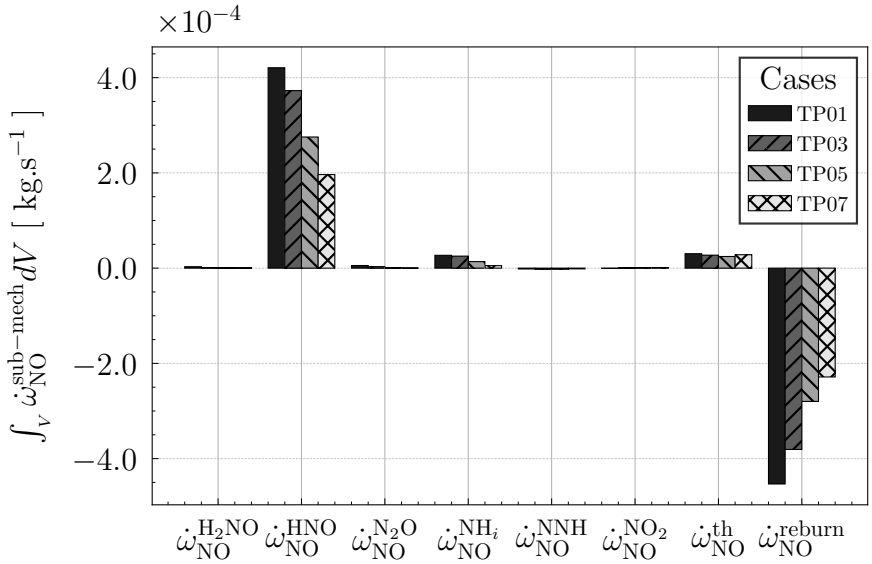

Figure 16: Volume-integrated NO production rates for different sub-mechanisms across operating conditions.

mechanism accounts for 89-91% of total NO production, while the NH_i route contributes 5-6%, showing a similar trend as the HNO route but with lower absolute magnitudes. The contributions of these two fuel-NO sub-mechanisms decrease as the mixture transitions from rich to lean conditions, consistent with the reduced availability of hydrogen radicals in fuel-lean environments. The thermal NO pathway, while present, contributes only 5-7% which is minimal compared to the fuel-bound nitrogen routes, reflecting the minimal temperature effects and the dominant role of ammonia-derived nitrogen chemistry. The remaining production routes, NO_2, N_2O and H_2NO, represent together less than 1%. One may expect higher N_2O production in TP01, since N_2O levels have been observed to dramatically increase for $\phi < 0.7$. This production, however, is not only due to the consumption of NO but to the presence of ammonia-linked radicals as well, as previously explained.

At first glance, NO production appears to be the highest at TP01, which seems contradictory when NO exhaust levels are known to reach their peak around $\phi = 0.8$. This, however, is easily explained by the significant contribution of the reburn (thermal $deNO_x$) sub-mechanism at TP01, which counterbalances the other NO production sub-mechanisms. Indeed, thermal $deNO_x$ dominates at over 99% of total consumption while NNH contributes 0.4-0.8% and NO_2 shows negligible net impact.

While the present study focuses on atmospheric pressure conditions, the implications of elevated pressure, as encountered in practical gas turbine applications, merit consideration. In NH_3-H_2 flames, experimental and numerical studies have consistently shown that NO mole fraction decreases as pressure increases [57, 58], a trend attributed to the enhanced importance of three-body recombination reactions that alter the radical pool composition and promote NO consumption. Specifically, third-body reactions such as NH + NO $\rightleftharpoons$ N_2O + M and NH_2 + NO $\rightleftharpoons$ N_2 + OH + M become more significant at elevated pressures, effectively converting NO into N_2 and N_2O [58]. This behavior is counterintuitive given the concomitant rise in flame temperature, and underscores the dominant role of chemical kinetics over thermal effects in driving NO formation in these flames, a conclusion that is fully consistent with the findings of the present work, wherein NO production is shown to be primarily kinetics-driven rather than thermally driven.

4. Conclusion

Finite rate chemistry LES were conducted to quantify and understand the effect of NO formation sub-mechanisms in ammonia-hydrogen swirled flames across multiple mean equivalence ratios.Numerical predictions demonstrated good agreement with available experimental PLIF NO measurements and OH* chemiluminescence imaging, thereby validating the numerical approach.

The impact of equivalence ratio on NO production was investigated. The differentiated injection strategy created fuel stratification and therefore multiple reaction zones with distinct NO formation characteristics.

This study demonstrates the intricate interplay between H_2 chemistry and NH_3 chemistry in the combustion of fuel blends. Compared to conventional hydrocarbon combustion, a change in equivalence ratio can drastically affect exhaust pollutant formation, sometimes by several orders of magnitude. Cell-by-cell analysis revealed that

the HNO route dominated NO production under all conditions, contributing approximately 90% of the global NO formation. Both the NH_i and the thermal pathway accounted for roughly 5-6% of the total NO produced. Conversely, the thermal-deNO_x route accounted for approximately 99% and of the total NO consumption.

NO formation in NH_3-H_2 flames exhibits high sensitivity to heat losses and equivalence ratio variations. Thus, accurate thermal boundary condition modeling is essential for predictive simulations, specially since thermal power is in direct correlation with heat losses, *i.e.*, academic studies at atmospheric pressure might not be representative of the actual heat losses at elevated thermal power and pressure. From this perspective, a quantitative assessment of pollutant formation remains to be explored, as it would require additional numerical efforts to account for accurate thermal boundary conditions. Future work should, therefore, prioritize the implementation of conjugate heat transfer (CHT) modeling strategy and systematic parametric studies examining the impact of wall thermal boundary conditions on NO_x emissions.

CRediT authorship contribution statement

HJVR: Writing - Original Draft, Conceptualization, Methodology, Validation, Formal analysis, Investigation, Data Curation, Visualization. **TN**: Writing – review & editing, Software, Formal analysis. **BA**: Investigation, Validation. **DL**: Writing – review & editing, Supervision. **GL**: Writing – review & editing, Supervision. **SM**: Resources, Investigation, Validation. **AV**: Writing – review & editing, Funding acquisition, Supervision, Project administration. **LG**: Writing – review & editing, Funding acquisition, Supervision, Project administration.

Declaration of competing interest

The authors declare that they have no known competing financial interests or personal relationships that could have appeared to influence the work reported in this paper.

Acknowledgments

The authors acknowledge funding from TotalEnergies and the ANRT through the CIFRE grant 2021/1492 as well as funding from the SAFE project (EP/T009314/1). The HPC resources from TotalEnergies' PANGEA 4 and GENCI-IDRIS (2024-A0172B10157) are acknowledged.

Supplementary Material

Supplementary Material is provided to support the presented results.

References

[1] C. W. Ong, N. Chang, M.-L. Tsai, C.-L. Chen, Decarbonizing the energy supply chain: Ammonia as an energy carrier for renewable power systems, Fuel 360 (2024) 130627.

[2] International Energy Agency, Global energy review 2025, Tech. rep., IEA, Paris, licence: CC BY 4.0 (2025).

[3] D. Pashchenko, Ammonia fired gas turbines: Recent advances and future perspectives, Energy 290 (2024) 130275.

[4] C. Mounaïm-Rousselle, P. Brequigny, Ammonia as fuel for low-carbon spark-ignition engines of tomorrow's passenger cars, Front. Mech. Eng. 6 (2020).

[5] C. Tornatore, L. Marchitto, P. Sabia, M. De Joannon, Ammonia as green fuel in internal combustion engines: State-of-the-art and future perspectives, Front. Mech. Eng. 8 (2022).

[6] X. Liu, Q. Tang, H. G. Im, Enhancing ammonia engine efficiency through pre-chamber combustion and dual-fuel compression ignition techniques, J. Clean. Prod. 436 (2024) 140622.

[7] A. Valera-Medina, H. Xiao, M. Owen-Jones, W. David, P. Bowen, Ammonia for power, Prog. Energy Combust. Sci. 69 (2018) 63–102.

[8] H. Kobayashi, A. Hayakawa, K. K. A. Somarathne, E. C. Okafor, Science and technology of ammonia combustion, Proc. Combust. Inst. 37 (2019) 109–133.

[9] T. Boningari, P. G. Smirniotis, Impact of nitrogen oxides on the environment and human health: Mn-based materials for the NOx abatement, Curr. Opin. Chem. Eng. 13 (2016) 133–141.

[10] G. Myhre, D. Shindell, F.-M. Bréon, et al., Anthropogenic and natural radiative forcing, in: Climate Change 2013: The Physical Science Basis. Contribution of Working Group I to the Fifth Assessment Report of the Intergovernmental Panel on Climate Change, Cambridge University Press, Cambridge, United Kingdom and New York, NY, USA, 2013, p. 659.

[11] Y. B. Zeldovich, The oxidation of nitrogen in combustion and explosions, Princeton University Press, 1992, p. 364–403.

[12] C. Fenimore, Formation of nitric oxide in premixed hydrocarbon flames, Symp. (Int.) Combust. 13 (1971) 373–380.

[13] A. L. Purohit, A. Nalbandyan, P. C. Malte, I. V. Novosselov, NNH mechanism in low-NOx hydrogen combustion: Experimental and numerical analysis of formation pathways, Fuel 292 (2021) 120186.

[14] J. W. Bozzelli, A. M. Dean, O + NNH: A possible new route for NOx formation in flames, Int. J. Chem. Kinet. 27 (1995) 1097–1109.

[15] P. C. Malte, D. T. Pratt, The role of energy-releasing kinetics in noxformation: Fuel-lean, jet-stirred CO-air combustion, Combust. Sci. Technol. 9 (1974) 221–231.

[16] E. Chui, A. Majeski, M. Douglas, Y. Tan, K. Thambimuthu, Numerical investigation of oxy-coal combustion to evaluate burner and combustor design concepts, Energy 29 (2004) 1285–1296.

[17] D. Shimokuri, S. Fukuba, S. Ishizuka, Fundamental investigation on the fuel-NO emission of the oxy-fuel combustion with a tubular flame burner, Proc. Combust. Inst. 35 (2015) 3573–3580.

[18] S. Mashruk, H. Shi, L. Mazzotta, C. E. Ustun, B. Aravind, R. Meloni, A. Alnasif, E. Boulet, R. Jankowski, C. Yu, M. Alnajideen, A. Paykani, U. Maas, R. Slefarski, D. Borello, A. Valera-Medina, Perspectives on NOx emissions and impacts from ammonia combustion processes, Energy Fuels 38 (2024) 19253–19292.

[19] B. Yan, Z. Wu, S. Zhou, J. Lv, X. Liu, W. Wu, G. Chen, A critical review of NH3–H2 combustion mechanisms, Renew. Sustain. Energy Rev. 196 (2024) 114363.

[20] T. Sano, NO2 Formation in the mixing region of hot burned gas with cool air, Combust. Sci. Technol. 38 (1984) 129–144.

[21] E. L. Merryman, A. Levy, Nitrogen oxide formation in flames: The roles of NO2 and fuel nitrogen, Symp. Int. Combust. 15 (1975) 1073–1083.

[22] A. Stagni, C. Cavallotti, H-abstractions by O2, NO2, NH2, and HO2 from H2NO: Theoretical study and implications for ammonia low-temperature kinetics, Proc. Combust. Inst. 39 (2023) 633–641.

[23] Q. Meng, L. Lei, J. Lee, M. P. Burke, On the role of HNNO in NOx formation, Proc. Combust. Inst. 39 (2023) 551–560.

[24] A. Katoch, T. F. Guiberti, D. V. de Campos, D. A. Lacoste, Dual-fuel, dual-swirl burner for the mitigation of thermoacoustic instabilities in turbulent ammonia-hydrogen flames, Combust. Flame 246 (2022) 112392.

[25] S. Mashruk, S. Zitouni, P. Brequigny, C. Mounaim-Rousselle, A. Valera-Medina, Combustion performances of premixed ammonia/hydrogen/air laminar and swirling flames for a wide range of equivalence ratios, Int. J. Hydrog. Energy 47 (2022) 41170–41182.

[26] D. Laera, P. Agostinelli, L. Selle, Q. Cazères, G. Oztarlik, T. Schuller, L. Gicquel, T. Poinsot, Stabilization mechanisms of ch4 premixed swirled flame enriched with a non-premixed hydrogen injection, Proc. Combust. Inst. 38 (2021) 6355–6363.

[27] S. Mashruk, E. Okafor, M. Kovaleva, A. Alnasif, D. Pugh, A. Hayakawa, A. Valera-Medina, Evolution of N2O production at lean combustion condition in NH3/H2/air premixed swirling flames, Combust. Flame 244 (2022) 112299.

[28] M. C. Franco, R. C. Rocha, M. Costa, M. Yehia, Characteristics of NH3/H2/air flames in a combustor fired by a swirl and bluff-body stabilized burner, Proc. Combust. Inst. 38 (2021) 5129–5138.

[29] X. Zhu, A. A. Khateeb, T. F. Guiberti, W. L. Roberts, NO and OH* emission characteristics of very-lean to stoichiometric ammonia–hydrogen–air swirl flames, Proc. Combust. Inst. 38 (2021) 5155–5162.

[30] S. Mashruk, M. Kovaleva, A. Alnasif, C. T. Chong, A. Hayakawa, E. C. Okafor, A. Valera-Medina, Nitrogen oxide emissions analyses in ammonia/hydrogen/air premixed swirling flames, Energy 260 (2022) 125183.

[31] A. Alnasif, S. Mashruk, M. Kovaleva, P. Wang, A. Valera-Medina, Experimental and numerical analyses of nitrogen oxides formation in a high ammonia-low hydrogen blend using a tangential swirl burner, Carbon Neutr. 1 (Jun. 2022).

[32] H. Vargas Ruiz, D. Laera, G. Lartigue, S. Mashruk, A. Valera-Medina, L. Gicquel, Extension of the dynamic thickened flame model for partially-premixed multi-fuel multi-injection combustion and application to an ammonia–hydrogen swirled flame, Combust. Flame 274 (2025) 113992.

[33] L. De Nardi, H. J. Vargas Ruiz, Q. Douasbin, O. Dounia, T. Poinsot, Les modeling of high-pressure nitrogen cross-flow jet impact on hydrogen-air deflagration, Proc. Combust. Inst. 40 (2024) 105263.

[34] E. Matas Mur, O. Dounia, O. Vermorel, Q. Douasbin, Impact of stratification and global mixture properties on flame acceleration: A numerical study, Int. J. Hydrog. Energy 101 (2025) 1267–1278.

[35] L. Gaipl, T. Poinsot, Confinement effects on a supersonic hydrogen jet flame in a duct, in: 12th European Combustion Meeting (ECM2025), Edinburgh, United Kingdom, 2025.

[36] A. Felden, P. Pepiot, L. Esclapez, E. Riber, B. Cuenot, Including analytically reduced chemistry (ARC) in CFD applications, Acta Astronaut. 158 (2019) 444–459.

[37] N. Rouland, T. Naess, E. Riber, B. Cuenot, Impact of detailed transport on the prediction of NOx formation in hydrogen–air flames, Fuel 392 (2025) 134830.

[38] C. R. Shaddix, A new method to compute the proper radiant heat transfer correction of bare-wire thermocouple measurements. (2017).
URL `https://www.osti.gov/biblio/1456686`

[39] A. G. Gaydon, The spectroscopy of flames, Springer, Dordrecht, Netherlands, 1974.

[40] T. Roose, R. Hanson, C. Kruger, A shock tube study of the decomposition of NO in the presence of NH3, Symp. (Int.) Combust. 18 (1981) 853–862.

[41] K. Ohashi, T. Kasai, D. Che, K. Kuwata, Alignment dependence of the amidogen chemiluminescence in the reaction of argon(3p) atoms with the aligned ammonia molecules, J. Phys. Chem. 93 (2002) 5484–5487.

[42] G. Schott, L. Blair, J. Morgan Jr, Exploratory shock-wave study of thermal nitrogen trifluoride decomposition and reactions of nitrogen trifluoride and dinitrogen tetrafluoride with hydrogen, J. Phys. Chem. 77 (2002) 2823–2830.

[43] Y. Yi, R. Zhang, L. Wang, J. Yan, J. Zhang, H. Guo, Plasma-triggered CH4/NH3 coupling reaction for direct synthesis of liquid nitrogen-containing organic chemicals, ACS Omega (2017).

[44] E. W. Hansen, P.-L. Law, Recursive methods for computing the abel transform and its inverse, J. Opt. Soc. Am. 2 (1985) 510.

[45] G. Wang, H. Tang, C. Yang, G. Magnotti, W. L. Roberts, T. F. Guiberti, Quantitative laser-induced fluorescence of NO in ammonia-hydrogen-nitrogen turbulent jet flames at elevated pressure, Proc. Combust. Inst. 39 (2023) 1465–1474.

[46] J. Luque, D. Crosley, LIFBASE Spectroscopy Tool, S.R.I. International (1999). URL `https://www.sri.com/platform/lifbase-spectroscopy-tool/`

[47] T. Schonfeld, M. Rudgyard, Steady and unsteady flow simulations using the hybrid flow solver AVBP, AIAA Journal 37 (1999) 1378–1385.

[48] P. D. Lax, B. Wendroff, Difference schemes for hyperbolic equations with high order of accuracy, Commun. Pure Appl. Math. 17 (1964) 381–398.

[49] F. Nicoud, H. B. Toda, O. Cabrit, S. Bose, J. Lee, Using singular values to build a subgrid-scale model for large eddy simulations, Phys. Fluids 23 (2011).

[50] T. Poinsot, S. Lele, Boundary conditions for direct simulations of compressible viscous flows, J. Comput. Phys. 101 (1992) 104–129.

[51] P. Agostinelli, D. Laera, I. Boxx, L. Gicquel, T. Poinsot, Impact of wall heat transfer in Large Eddy Simulation of flame dynamics in a swirled combustion chamber, Combust. Flame 234 (2021) 111728.

[52] F. Charlette, C. Meneveau, D. Veynante, A power-law flame wrinkling model for LES of premixed turbulent combustion part I: non-dynamic formulation and initial tests, Combust. Flame 131 (2002) 159–180.

[53] T. Jaravel, Prediction of Pollutants in Gas Turbines using Large Eddy Simulation, PhD Thesis, Université de Toulouse - École doctorale MEGeP (2016).

[54] H. Yamashita, M. Shimada, T. Takeno, A numerical study on flame stability at the transition point of jet diffusion flames, Symp. (Int.) Combust. 26 (1996) 27–34.

[55] A. Cellier, Large Eddy Simulation of lithium-ion battery fires for the diagnostic of thermal runaway, PhD Thesis, Université de Toulouse - École doctorale MEGeP (2023).

[56] A. Stagni, C. Cavallotti, S. Arunthanayothin, Y. Song, O. Herbinet, F. Battin-Leclerc, T. Faravelli, An experimental, theoretical and kinetic-modeling study of the gas-phase oxidation of ammonia, React. Chem. Eng. 5 (2020) 696–711.

[57] A. Hayakawa, T. Goto, R. Mimoto, T. Kudo, H. Kobayashi, NO formation/reduction mechanisms of ammonia/air premixed flames at various equivalence ratios and pressures, Mech. Eng. J. 2 (1) (2015) 14–00402–14–00402.

[58] S. Wang, Z. Wang, A. M. Elbaz, X. Han, Y. He, M. Costa, A. A. Konnov, W. L. Roberts, Experimental study and kinetic analysis of the laminar burning velocity of NH3/syngas/air, NH3/CO/air and NH3/H2/air premixed flames at elevated pressures, Combust. Flame 221 (2020) 270–287.